Pattern production through a chiral chasing mechanism

Thomas E. Woolley

Phys. Rev. E **96**, 032401 — Published 1 September 2017

DOI: 10.1103/PhysRevE.96.032401

Pattern production through a chiral chasing mechanism

Thomas E. Woolley
Cardiff School of Mathematics Cardiff University, Senghennydd Road, Cardiff, CF24 4AG
(Dated: August 14, 2017)

Recent experiments on zebrafish pigmentation suggests that their typical black and white striped skin pattern is made up of a number of interacting chromatophore families. Specifically, two of these cell families have been shown to interact through a non-local chasing mechanism, which has previously been modelled using integro-differential equations. We extend this framework to include the experimentally observed fact that the cells often exhibit chiral movement, in that the cells chase, and run away, at angles different to the line connecting their centres. This framework is simplified through the use of multiple small limits leading to a coupled set of partial differential equations which are amenable to Fourier analysis. This analysis results in the production of dispersion relations and necessary conditions for a patterning instability to occur. Beyond the theoretical development and the production of new pattern planiforms we are able to corroborate the experimental hypothesis that the global pigmentation patterns can be dependent on the chirality of the chromatophores.

I. INTRODUCTION

Developmental systems are able to create and sustain a wide variety of patterns, from digit formation [1] to animal skin pigmentation [2]. However, despite decades of research, an experimentally tested mechanistic theory of developmental pattern formation still eludes us [3].

Many mathematical theories of pattern formation exist [4], some are hydrodynamic in behaviour [5], whilst others look at a more mechanical descriptions of domain boundaries, resulting in cellular patterns [6]. Perhaps the most successful theory of patterning stems from Alan Turing's seminal work on the chemical theory of morphogenesis [7], which showed that two distinct diffusible populations (known as morphogens) could produce stationary heterogeneous spatial patterns if the interactions of the two populations satisfied specific criteria. Pluripotent cells would then be able to detect the heterogeneous morphogen distribution and differentiate based on the local environment, giving rise to differentiated and, hence, patterned structures [8]. This theory was highly counter-intuitive because the interaction conditions assume that in the absence of diffusion the population densities would evolve to a stable and stationary value. Thus, it is diffusion (which is normally thought of as a homogenising process) that drives the system to spatial heterogeneity [9]. Since Turing's original work, his theory has been extended in multiple directions [10, 11] including higher order networks, stochastic effects and delays [12–17].

Turing's morphogens are usually thought to be diffusible proteins. However, although there are a number of potential candidates for putative morphogens (e.g. TGF-β, WNT, DKK [18, 19] and Hox genes [20]) the hunt for the first conclusive developmental evidence of a Turing structure at the molecular level continues. More recently, experimental work has suggested that the morphogens may be the cells themselves, rather than the cells reading chemical gradients [21–23].

Specifically, it has been suggested that the black and white stripes of the zebrafish may be formed due to the movement and interactions of three types of pigment cells, known as chromatophores. The dark stripes of the pattern consist of melanophores (black cells containing melanin granules) and iridophores (silvery and/or white cells containing ultra-fine reflecting platelets), whilst the light stripes consist of xanthophores (yellow to orange cells containing pteridine and carotenoid granules) and iridophores [24, 25].

When the melanophores and xanthophores are extracted and plated together they are seen to interact and move relative to one another. In particular, wild-type xanthophores move more slowly than melanophores. However, the xanthophores are able to extrude long pseudopodia which, on contact with a melanophore, induce the xanthophore to move closer to the melanophore, whilst the melanophore is induced to move away from the xanthophore, resulting in a chasing form of motion. Critically, the movement direction of the xanthophores and melanophores is not along the line connecting their cell centres. Indeed, their directed motions can be rotated at a significant angle away from this line (see Figure 1) [26–28]. Moreover, the pigment cells of mutant fish are seen to exhibit different behaviours and different patterns, suggesting a correspondence between microscale cell behaviour and mesoscale patterning of the skin.

Including the attraction-repulsion dynamics suggested by the experimental observations into the standard reaction-diffusion framework has already been done by Painter, Sherratt and coauthors [29, 30] and their research shows that such a chasing mechanism cannot support stationary heterogeneity without the addition of further assumptions, confirming the earlier result of Woolley et al. [27]. Here, we will extend their work by including the rotational disparity of the chasing and evading agents. It should be noted that although we use the zebrafish pigmentation observations as a motivating example this paper focuses on introducing the modelling framework and illustrating the diversity of patterns contained within. However, we are able to generate the conclusion that the global pattern does depend on the microscale angles, as suggested by Kondo's experiments [31].

In Section II we derive the basic framework from a two-dimensional space-jump model in a complementary approach to [32]. Standard linearisation arguments and Fourier analysis are used to derive conditions under which patterns can form and these are shown to hold through numerical simulations in Section III. Finally, we summarise the variety of different dynamics exhibited in Section IV.

II. FRAMEWORK

Although we will initially not be considering the influence of diffusion in the results section, as we will be focusing on the angular chasing mechanism, we will include diffusive movement later in Section III A 3. The inclusion of diffusion is in order to understand how this additional movement process effects the patterns produced by the angular chasing mechanism. Equally, it allows us to introduce the reader to the modelling framework through a familiar example. The diffusion operator is derived in Appendix A.

We now consider the situation of angular chasing, where the motion of the populations is no longer independent of location, but rather the motion of one population depends on the surrounding densities of another population. Specifically, we consider the following set up: two continuous cell populations, u and v, in an infinite domain two-dimensional domain are able to nonlocally interact over a range R, which mirrors the non-local interaction abilities of the cells in the zebrafish. When the cells of type u sense the cells of type v they move a distance r_{1x} horizontally and r_{1y} vertically, such that the movement vector makes a fixed angle θ_1, against the line joining the cells, measured in an anti-clockwise manner. Similarly, the v cells respond by moving a distance r_{2x} and r_{2y} producing a fixed angle θ_2 (see Figure 1).

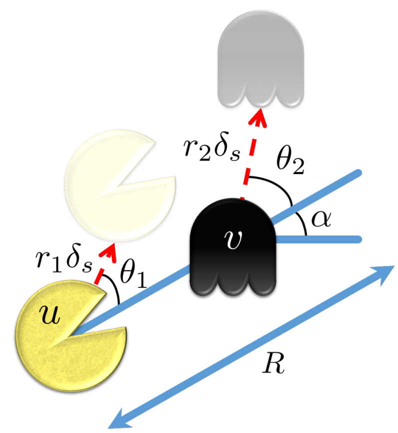

FIG. 1. When the centres of two individuals from different populations come within a distance R of one another the cell of type u will move a distance $r_1\delta_s$ towards the cell of type v, whilst the cell of type v will move a distance $r_2\delta_s$ away from u. Note that δ_s is some spatial length scale used to discretise the space, whilst r_1/r_2 measures the ratio of movement distance between the two species. Complicating matters further is the fact that the populations u and v do not move along the line joining their centres. Instead, the populations u and v travel at angles θ_1 and θ_2, respectively, to this line. Initially, we consider the populations moving on an infinite domain.

For total accuracy we should start the modelling at the individual scale of the cells using a stochastic formalism and derive mean-field limit differential equations, which define the densities. However, assuming that the patterning process involves a large number of cells we can appeal to the weak noise limit [33], meaning that we can effectively use individuals and density interchangeably, as they are approximately proportional.

The time evolution equation for this system defines the net flux of population density at a given point, (x, y). Each species' flux is made up of two components, the rate at which the cells jump to the given point and the rate at which the cells jump from the given point. For example, using the Law of Mass Action, the flux of population u

away from (x, y) is proportional to the product of the density of u at (x, y) at time t (*i.e.* $u(x, y, t)$) and the density of v at some point within a circle of radius R of (x, y) at time t. Defining $r \in [0, R]$, $\alpha \in [0, 2\pi]$ and $j > 0$ to be the constant of proportionality then the interaction equation of the flux of u away from (x, y) is given by the following interaction equation (compare with equation (A1))

$$\begin{aligned} &v(x + r\cos(\alpha), y + r\sin(\alpha)) + \\ &u(x, y) \xrightarrow{j} u(x + r_{1x}, y + r_{1y}) + \\ &v(x + r\cos(\alpha) + r_{2x}, y + r\sin(\alpha) + r_{2y}), \end{aligned} \quad (1)$$

where r_{il}, $i \in \{1, 2\}$, $l \in \{x, y\}$, have the specific form $r_{1x} = r_1\delta_x \cos(\theta_1)$ and $r_{1y} = r_1\delta_y \sin(\theta_1)$, with r_{2x} and r_{2y} defined similarly. Later we will fix $\delta_x = \delta_y = \delta_s$ justifying the variables illustrated in Figure 1. Further, we should note that equation (1) holds for all $r \in [0, R]$ and $\alpha \in [0, 2\pi]$. Finally, the time dependence is suppressed in the above and following derivation for brevity.

Using the Law of Mass Action on equation (1) and integrating over the circle or radius R, centred at (x, y) means that the flux of u out of the point (x, y) is given by

$$\int_0^{2\pi} \int_0^R j u(x, y) v(x + r\cos(\alpha), y + r\sin(\alpha)) r \, \mathrm{d}r \, \mathrm{d}\alpha, \quad (2)$$

where we note that the flux has the form of an integral because the interactions can occur at any point within the circle of radius R. Further details can be found in Appendix B.

In order to simplify the evolution equations we assume that the radius of detection is small, namely $R = \delta_s$, and take the limit of $R = \delta_x = \delta_y = \delta_s$ tending to zero. In Appendix C it is demonstrated how Taylor expanding the resulting integro-differential equations, setting $J = \delta_s^4 j\pi/3$ to remain constant and taking the limit $\delta_s \to 0$ leads to the following closed system of partial differential equations (PDEs),

$$\frac{\partial u}{\partial t} = \frac{3Jr_1^2}{4}\nabla^2(uv) - r_1 J \nabla \cdot (u\boldsymbol{M}(\theta_1)\nabla v), \quad (3)$$

$$\frac{\partial v}{\partial t} = \frac{3Jr_2^2}{4}\nabla^2(uv) + r_2 J \nabla \cdot (v\boldsymbol{M}(\theta_2)\nabla u), \quad (4)$$

where

$$\boldsymbol{M}(\theta) = \begin{pmatrix} \cos(\theta) & -\sin(\theta) \\ \sin(\theta) & \cos(\theta) \end{pmatrix} \quad (5)$$

is the standard two-dimensional rotation operator.

If we consider equation (3) (with analogous insights holding for equation (4)) we see that $\nabla^2(uv)$ is the local sensing term, whilst the $\nabla \cdot (uM(\theta)\nabla v)$ term is the non-local sensing term, in that u is sensing the gradient in v. This can be seen in the case that we consider v to be initially a uniform field. In this case $\nabla v = 0$, but there should still be movement, which corresponds to the term $\nabla^2(uv)$, *i.e.* random motion, with a diffusion rate proportional to the v concentration. Further, $\nabla^2(uv)$ does not contain an angle dependent term because if the two cells are at the same point there cannot be a preferred direction. The first term does not appear in the work of Painter, Sherratt and co-authors [29, 30] as they only consider non-local interactions.

In the production of equations (3) and (4) we have used many small scale approximations. Preliminary stochastic, individual based simulations suggest that at least some of the patterns present in the continuum case (see Section III) are present in the discrete case too (data not shown). However, the rigorous demonstration of this fact is still in its infancy and the author intends to return to this question as a subject of future work.

A. Additional reactions

As we will see later the rotational dispersion as defined in Section II cannot solely support patterning, thus we include local interactions defined by the functions $f(u, v)$ and $g(u, v)$, which can simply be added to equations (3) and (4). The functions f and g model the kinetic terms and are, thus, usually non-linear. Whence, as seen in Appendix D, we are able to apply the standard Turing linear stability analysis, in order to derive conditions under which patterning occurs. Specifically, in Appendix D, we assume that in the absence of motion, $J = 0$, there is a stable steady state, (u_0, v_0) satisfying $f(u_0, v_0) = g(u_0, v_0) = 0$, whilst in the presence of motion, $J > 0$, we derive sufficient conditions that cause this steady state to be linearly unstable, resulting in a motion-driven instability that drives the system into a heterogeneous state. Although the linear stability analysis demonstrates that the uniform steady state is unstable, we have to carefully choose non-linear terms in order to bound the heterogeneous solution.

From Appendix D we discover that the a patterning instability requires us to satisfy the following inequalities,

$$\begin{aligned}
&f_u + g_v < 0, && (6)\\
&f_u g_v - f_v g_u > 0, && (7)\\
&4\cos(\theta_1)\cos(\theta_2) - 3r_1\cos(\theta_2) + 3\cos(\theta_1) r_2 > 0, && (8)\\
&\left(\left(r_2\left(4\cos(\theta_2) + 3r_2\right) f_v - 3{r_1}^2 g_v\right)\frac{v_0}{4} - \left(r_1\left(4\cos(\theta_1) - 3r_1\right) g_u + 3 f_u {r_2}^2\right)\frac{u_0}{4}\right) < \\
&- \sqrt{r_1 r_2\left(4\cos(\theta_1)\cos(\theta_2) + 3\cos(\theta_1) r_2 - 3r_1\cos(\theta_2)\right) u_0 v_0 \left(f_u g_v - f_v g_u\right)}. && (9)
\end{aligned}$$

Inequalities (6) to (9) are denoted patterning conditions $P1 - P4$, respectively, and form the four critical stability conditions that will keep the steady state stable in the absence of motion, but be driven to instability when motion is incorporated.

Here, we note a few key observation about the conditions $P1 - P4$:

1. If interactions are not considered, $f = g = 0$, then no unstable frequencies can exist in the presence of motion (as seen from equations (D4) and (D5)), hence, no patterns can form. Thus, reactions are required in this framework.

2. Since the four criteria depend (at most) only on the cosine of the angles then any stability criterion derived for (θ_1, θ_2) would also hold for $(-\theta_1, \theta_2)$, $(\theta_1, -\theta_2)$ and $(-\theta_1, -\theta_2)$. Hence, we can restrict our analysis to the interval $(\theta_1, \theta_2) \in [0, \pi] \times [0, \pi]$.

3. Condition $P3$ depends solely on the geometric variables $(r_1, r_2, \theta_1, \theta_2)$. Further, $P3$ is illustrated for multiple values of (r_1, r_2) in Figure 2 and, so, we observe that the valid patterning values of (θ_1, θ_2) are highly restricted. Critically, depending on the values of (r_1, r_2) there can be two disjoint regions of (θ_1, θ_2) that are not admissible (Figure 2(a)) or just one region (Figure 2(b)). Presently, we focus on the single region form and, thus, we are able to rearrange P3 to provide the single-valued inequality
$$\theta_2 > \max\left\{0, \arccos\left(\frac{3r_2\cos(\theta_1)}{3r_1 - 4\cos(\theta_1)}\right)\right\}.$$

4. For all values of r_1 and r_2, the 'high-θ_1-low-θ_2' parameter region is always outside of the region defined by $P3$. Note that high and low angles are used to colloquially define appropriate regions of the interval $[0, \pi]$. For an example 'high-θ_1-low-θ_2' see the white region of Figure 2(b). The interpretation of this region is that the 'chaser' and 'chased' cells run away from one another, as each interaction will lead to a wider separation than their previous states. Intuitively, under these conditions, no pattern can form.

5. Since inequality $P3$ depends only on r_1, r_2, θ_1 and θ_2 the geometry of the chasing cells fundamentally influences the stability of the system, independently of the interaction functions f and g. This means that it is possible to set the chasing dynamic parameters, $(r_1, r_2, \theta_1, \theta_2)$, in such a way that the system will never pattern, regardless of the interaction functional forms.

6. None of the four inequalities depend on the reaction rate parameter J, thus, instability is possible no matter how slow the interactions occur, as long as J is positive.

7. As we will see in Section III patterns can arise when $\theta_1 = \theta_2$. Equally, patterns are possible when $r_1 = r_2$.

8. The previous two points highlight one of the key differences between the requirements of curved chasing and Turing patterns. Specifically Turing patterns demand that the diffusion coefficients of the two morphogen populations are widely different. Here, the movement rate and geometry of the chasing

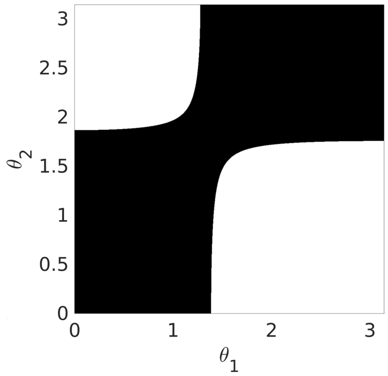

(a) $r_1 = 0.3$, $r_2 = 0.3$.

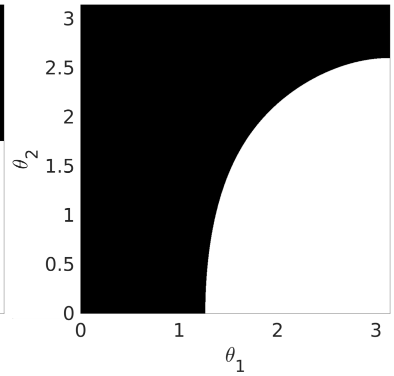

(b) $r_1 = 1$, $r_2 = 2$.

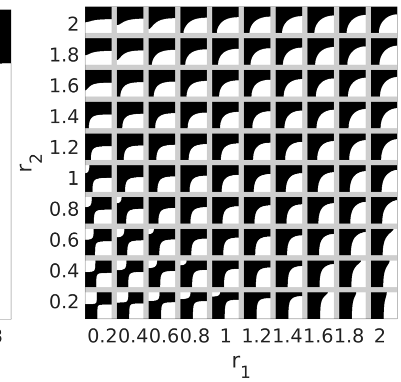

(c)

FIG. 2. Illustrating condition $P3$ for different values of r_1 and r_2. In (a) and (b) the black region shows where $P3$ is satisfied for specific examples of (r_1, r_2) noted beneath each figure, respectively. (c) illustrates multiple different possible configurations of the (θ_1, θ_2) space. Each small square represents inequality condition $P3$ evaluated over $(\theta_1, \theta_2) \in [0, \pi] \times [0, \pi]$ with the corresponding values of r_1 and r_2 shown on the axes. The values of r_1 and r_2 range over all possible combinations of $\{0.2, 0.4, 0.6, 0.8, 1, 1.2, 1.4, 1.6, 1.8, 2\}$.

and chased populations can all be the same and patterns will still occur.

9. The most likely chosen wave mode can be derived from the dispersion relation in Appendix D. Critically, although it will be dependent on the first derivatives and steady states of the functional forms it can be seen that frequencies will also be proportional to $J^{-1/2}$. Thus, even if the reaction kinetics and geometry of the chasing dynamics are fixed, we will still have explicit control over the pattern wavelength through the reaction rate, J.

III. RESULTS

In this section we look at multiple kinetic forms and even add diffusion into the system. Our goal is to illustrate not only the pattern forms that are possible, but also demonstrate how the rotational motion offers new types of previously unseen dynamics. Note that because we are application independent, all variables and results are in arbitrary consistent units. Since we have seen that the instability is independent of J then throughout the results section we fix $J = 1$. Equally, since we want to maintain a large (θ_1, θ_2) parameter region we fix $r_1 = 1$, $r_2 = 2$, which produces a parameter region as seen in Figure 2(b). Thus, we are left with only a minority of angles in the 'high-θ_1-low-θ_2' region that are unable to pattern.

It should be noted that the analysis in Section II and Appendix D does not include the influence of boundary conditions. Including boundaries simply restricts the frequencies, k, that can appear. However, unless the wave modes are highly constrained this extra restriction does not help specify what pattern (*e.g.* spots, stripes, stationary or non-stationary) is likely to appear in the full non-linear case as there are usually too many patterning modes available to accurately predict which one will be chosen by the random initial conditions. Thus, we depend on the insights provided by simulations as to the influence of the boundary upon the solution. Specifically, we will alter the simulation domain geometry to include circles and squares and vary the boundary conditions to include both zero-flux, periodic and mixed conditions.

Finally, it should be reiterated that the Schnakenberg kinetics, presented in Section III A, and the kinetics derived later are chosen on an ad-hoc basis. Specifically, we choose a variety of prototypical patterning kinetics to demonstrate the diversity of available patterns rather than focus on a single experimentally motivated case.

A. Schnakenberg kinetics

The first set of kinetics we consider are a modified form of Turing kinetics known as the

Schnakenberg system [34]

$$f = \alpha - u + u^2 v - \epsilon u^3, \tag{10}$$

$$g = \beta - u^2 v - \epsilon v^3. \tag{11}$$

Note that in addition to the standard kinetics a non-linear term with coefficient $\epsilon > 0$ has been subtracted from each interaction function. In the case that $\epsilon = 0$ it can be shown that the Schnakenberg kinetics are either stable or have limit cycle behaviour, depending on the coefficients α and β [34, 35]. Critically, the kinetics never cause either population density to blow up. Thus, by subtracting a cubic non-linearity of each population from their, respective, interaction functions we not only preserve the positivity of a solution (*i.e.* a solution beginning with $u, v > 0$ will always remain in the positive population quadrant) but also the populations are further constrained to exhibit finite bounded solutions for all time (*i.e.* blow up will not occur).

The above arguments only work in the case that we ignore space and treat the kinetics as functional forms for ordinary differential equations. Once spatial motion is considered, we can no longer guarantee finite populations for all time, which is why the cubic terms are subtracted from the kinetics. The idea is that if any population begins to increase without bound then the negative cubic terms will dominate the equations and cause the equations (10) and (11) to be negative, resulting in a negative time derivative for large population and, hence, a reduction in the population. Hence we contradict the assumption that a population could grow without bound. We then assume that the argument holds similarly in the spatially extended case.

Assuming $\epsilon \ll 1$ conditions $P1$–$P4$ take the form

$$P1: \quad 0 < 1 + (\alpha+\beta)^2 - 2\frac{\beta}{(\alpha+\beta)}; \tag{12}$$

$$P2: \quad 0 < (\alpha+\beta)^2; \tag{13}$$

$$P3: \quad 0 < 4\cos(\theta_1)\cos(\theta_2) + 6\cos(\theta_1) - 3\cos(\theta_2); \tag{14}$$

$$P4: \quad 2\left(\cos(\theta_1) + \cos(\theta_2)\right) - \frac{15}{4} + 3\frac{(\alpha+\beta)}{\beta} < -\sqrt{\frac{2(\alpha+\beta)}{\beta}\left(4\cos(\theta_1)\cos(\theta_2) + 6\cos(\theta_1) - 3\cos(\theta_2)\right)}. \tag{15}$$

Firstly, we note that $P2$ is always trivially satisfied, the other three conditions depend on $(\alpha, \beta, \theta_1, \theta_2)$.

In Figure 3 we illustrate the kinetic and angular inequalities separately. For fixed values of (θ_1, θ_2) we observe that the patterning region in the (α, β) plane is unbounded. In particular, for any given value of α we can always choose β big enough to satisfy $P4$. However, given fixed values of (α, β) the viable region in the (θ_1, θ_2) parameter space is much smaller. Critically, $\pi/2 < \theta_1, \theta_2 < \pi$, thus, in terms of the interpretation of the angles the 'chaser' would actually be running away from the 'chased', whilst the 'chased' would be running towards the 'chaser', *i.e.* the roles would appear to be reversed.

Figure 4 illustrates the patterns possible when parameters are chosen in the unstable regions of Figure 3. We clearly observe that standard spot patterns are able to form, similar to a Turing pattern. However, although the pattern is stable in terms of the number and size of spots the patterns in figures 4(a) and 4(b) are able to slowly process around their circular domain. Specifically, we mark a spot on the outer ring with an asterisk and a spot on the inner ring with an arrow head. These track their respective spots and aid in the visualisation of rotation. Critically, in both figures 4(a) and 4(b) the outer ring of spots rotates in a clockwise manner. This contrasts with the inner ring of spots which rotates anti-clockwise in Figure 4(a), but does not move in Figure 4(b). The only difference between these two simulations is the size of the domain. In Figure 4(a) the radius is 11 and is able to sustain 12 spots in the outer ring and five in the inner ring. This can be compared with Figure 4(b), which has radius 12 and is able to support 13 spots in

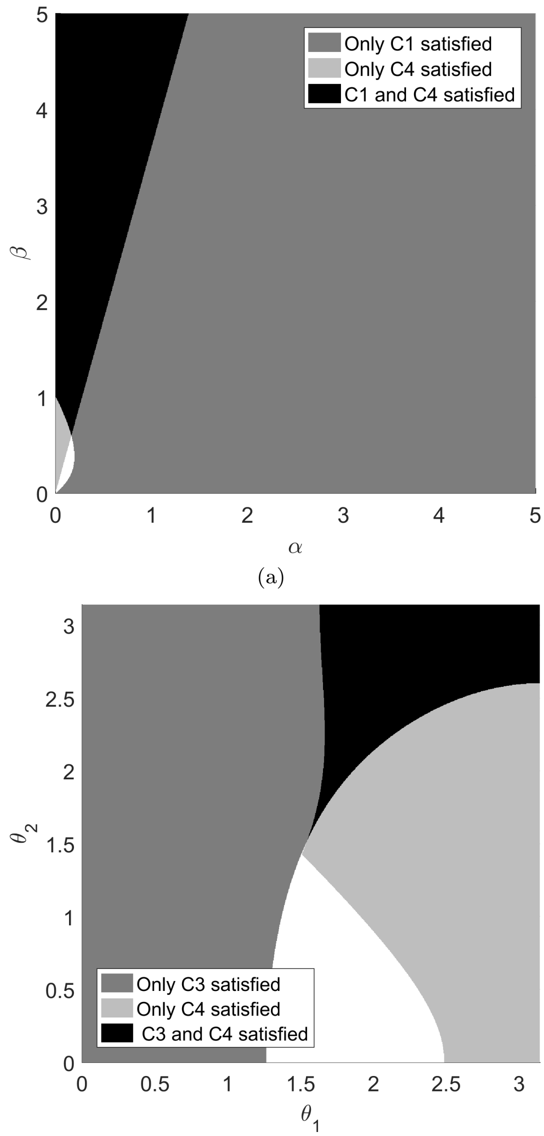

(a)

(b)

FIG. 3. Possible parameter regions for a patterning instability to occur in the Schnakenberg kinetics. (a) The feasible (α,β) parameter region when $(\theta_1,\theta_2) = (1.8, 2.2)$, note condition $P2$ is satisfied everywhere under these kinetics. (b) The feasible (θ_1,θ_2) parameter region when $(\alpha,\beta) = (0.1, 0.9)$.

the outer ring, 6 hexagonally packed spots in the inner ring and 1 central spot.

These rotating patterns can be further compared with Figure 4(c), which illustrates the exact same simulation but on a square domain of side length 20. Now the pattern evolves to a stationary stable state. Overall, we are able to use Figure 4 to clearly show that the boundary of the simulation has a critical influence on the evolution of the patterned state.

Following on from this we then consider the impact of the kinetics of the simulation. As noted in Figure 3(a), patterns can always be formed for large enough values of β. Thus, in Figure 5 we illustrate the influence of increasing β, whilst keeping all other parameters, initial conditions and boundary conditions the same. For small values of β we find only stationary structures and a transition from spots to stripes that matches the insights gained from a standard Turing pattern (see figures 5(a)-5(d)). However, for large enough β the system forms a central region of low density surrounded by a high density 'ring'. This high density ring then has multiple thin 'tendrils', or 'arms' of high density linking it to the boundary. The number of tendrils is dependent on β. Once this pattern is formed it appears to process stably in a clockwise manner, even though we are on a square domain (see figures 5(e) and 5(f)).

1. *Periodic boundary conditions*

Figure 5 demonstrated that the patterns are highly sensitive to boundary geometry. In this section we briefly investigate the influence of changing the boundary conditions. Specifically, we simulate the exact same system as that seen in Figure 5, but the left and right boundary conditions are periodically identified and the top and bottom boundaries are periodically identified. Thus, the simulations are topologically on a torus.

When $\beta = 1.4$ a stationary, regular array of spots is produced, similar to that seen in Figure 5(a) (data not shown). Equally, when $\beta = 2.3$ the simulation simply converges to a stationary labyrinthine pattern, similar to that seen in Figure 5(c) (data not shown). However, the cases of $\beta = 1.9$, 3.2, 3.7 are quite different. Specifically, the rotating patterns of figures 5(e) and 5(f) become stationary labyrinthine patterns that produce an approximately hexagonal grid (data not shown). Further, the $\beta = 1.9$ case does not seem to converge to a steady state (see Figure 6(a)), rather the labyrinthine patterns appears to constantly evolve, writhe and twist. Finally, although the $\beta = 3.2$ case appears to settle into a final labyrinthine pattern the global pattern is not stationary. Critically, it is seen to slowly drift down the domain (compare the left and right im-

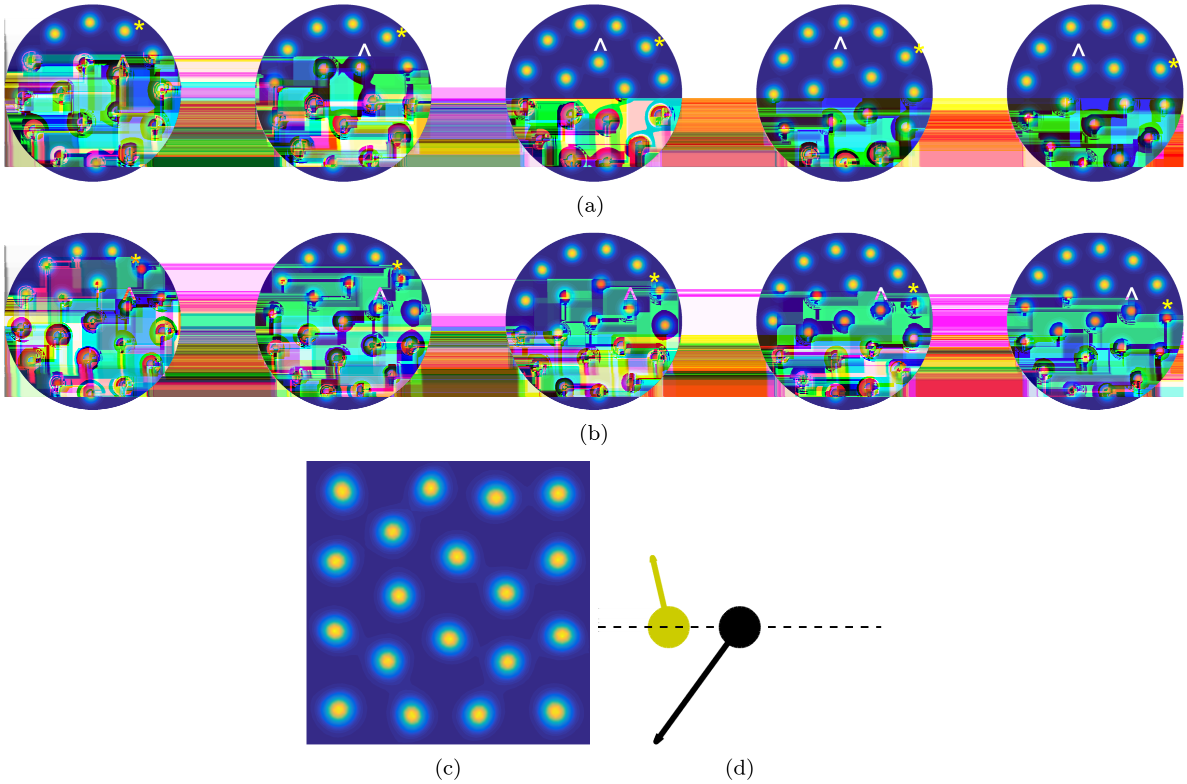

FIG. 4. Patterns present at one parameter set of the Schnakenberg kinetics (without diffusion). (a) and (b) present five different time points of the simulation, $t = 3000, 3500, 4000, 4500, 5000$. The figures illustrate a stable rotating pattern that appears on circular domains of radius (a) 11 and (b) 12. The yellow asterisk and white arrow head indicate the motion of a particular spot, thus making the rotation easier to see. (c) presents the equations solved on a square domain (side length 20), with the same parameter values and boundary conditions as (a) and (b). The pattern in (c) is stationary. (d) illustrates the relative angles and distance of the cell movement. The qualitative motion of the u population is given by the light yellow cell on the left, whilst the dark black cell on the right illustrates the qualitative motion of the v population (*c.f.* Figure 1). In this, and all other schematic images, the angles, θ_1 and θ_2, are measured relative to the dashed, horizontal line joining their cell centres. Parameters are $\alpha = 0.1$, $\beta = 0.9$, $\epsilon = 10^{-2}$ $\theta_1 = 1.8$, $\theta_2 = -2.2$, boundary conditions are zero-flux everywhere and the same uniformly distributed random initial initial conditions were used in each simulation. The pseudo-colour scale spans 7 (arbitrary units) in the spot peak to 0.1 (arbitrary units) in the trough, inter-spot region. See Supplemental Material at [URL will be inserted by publisher] for an animation of (a).

ages of Figure 6(b)).

2. *Mixed boundary conditions*

Having simulated both zero-flux and periodic boundary conditions separately, we now seek to combine the influences in this section. Specifically, Figure 7 simulates the exact same kinetics, initial conditions and parameter values as in Section III A, except that the zero-flux boundary condition is only defined on the left and right boundaries. The top and bottom boundaries are assumed to be periodic. Thus, the simulations are topologically on a cylinder. Each subfigure of Figure 7 illustrates increasing time points (see caption) demonstrating pattern evolution.

Intriguingly, the simulations outcomes are quite different from either of the cases in which the boundary conditions are purely zero-flux, or purely periodic. Specifically, although the patterns transitions between spots and stripes at broadly the same values of β (compare figures 5 and 7) the patterns are able to constantly evolve in unusual ways.

Figure 7(a) illustrates a simulation of moving

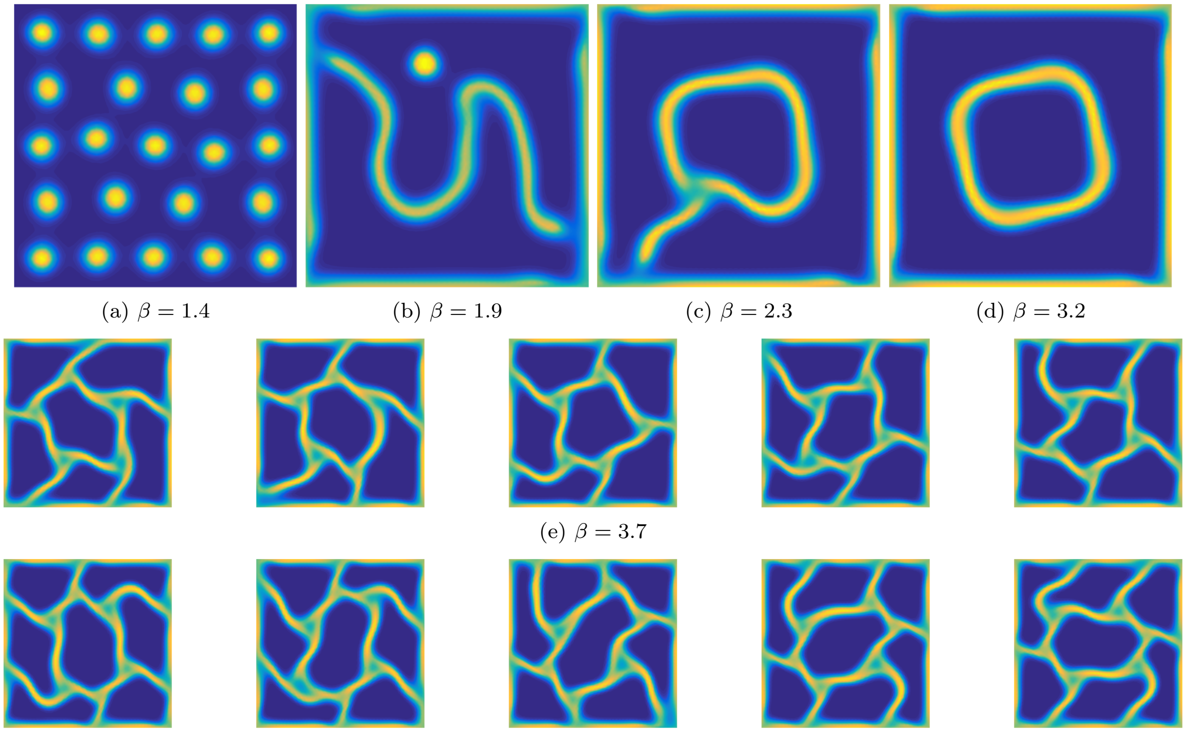

(a) $\beta = 1.4$ (b) $\beta = 1.9$ (c) $\beta = 2.3$ (d) $\beta = 3.2$

(e) $\beta = 3.7$

(f) $\beta = 4.1$

FIG. 5. A parameter sweep of the Schnakenberg kinetics (without diffusion) over β. Patterns (a)-(d) are stationary, whilst (e) and (f) produce stable rotating 'rings' with five and six 'arms', respectively. Parameters are the same as in Figure 4 except for β, which is noted beneath each subfigure. See Supplemental Material at [URL will be inserted by publisher] for an animation of (f).

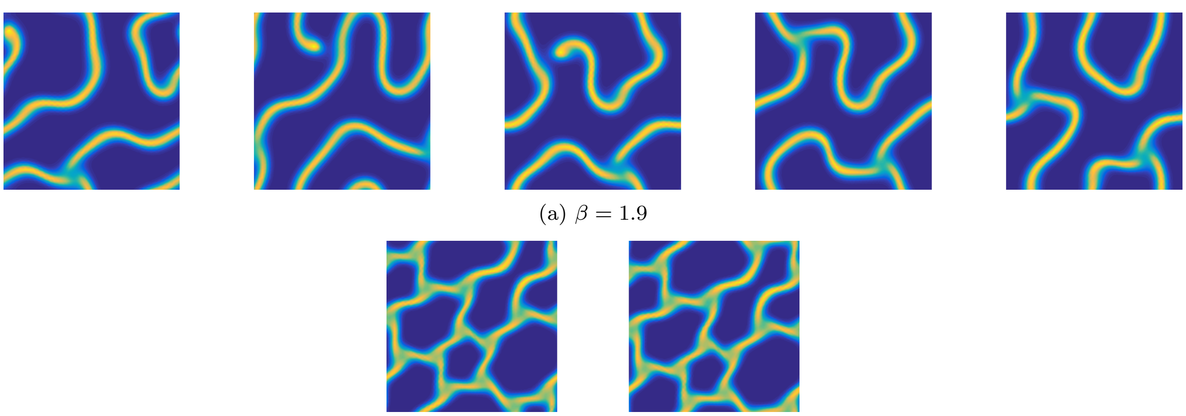

(a) $\beta = 1.9$

(b) $\beta = 3.2$

FIG. 6. Simulations from figures 5(b) and 5(d) repeated, but with periodic boundary conditions linking the left and right boundaries, as well as the top and bottom boundaries. (a) Time points shown (left to right) are 210, 300, 650, 850 and 1000. (b) Time points shown (left to right) are 600 and 1000. Parameters and all other conditions are the same as Figure 5 except for β, which is noted beneath each subfigure. See Supplemental Material at [URL will be inserted by publisher] for an animation of (a).

spots, however, the spots do not all move in the

same direction. The three left-hand spot columns

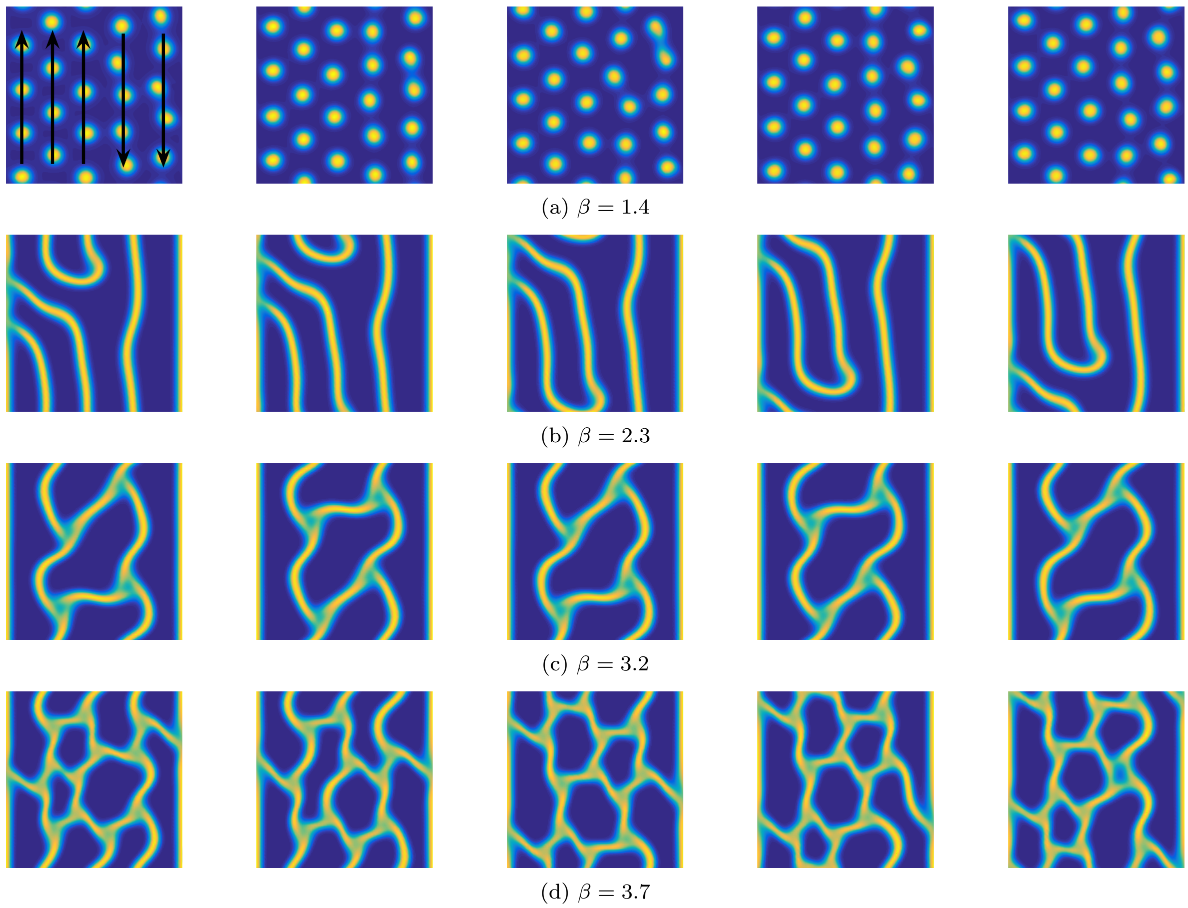

FIG. 7. Simulations from Figures 5(a), 5(c), 5(d) and 5(e) repeated, but with mixed boundary conditions. Specifically the top and bottom boundaries are linked periodically, whilst the left and right boundaries have zero-flux boundary conditions. Time points shown (left to right) are: (a) 280, 350, 420, 490 and 560; (b) 400, 450, 500, 550, 600; (c) and (d) 400, 480, 560, 640, 720. Parameters and all other conditions are the same as Figure 5. The β parameter is noted beneath each subfigure. See Supplemental Material at [URL will be inserted by publisher] for an animation of (a) and (d).

travel up the domain with a consistent hexagonal planiform. The two right-hand columns travel down the domain (see the illustrated black arrows on Figure 7(a)) but their spacing is much less consistent and the spots often coalesce and split apart (see the top right of the centre image of Figure 7(a) for an example of spot splitting). Here the 'shuttling' movement dynamics of the spots can be compared with the simulations from Section III A and Section III A 1, where it was noted that in both cases the spot patterns were stationary.

When $\beta = 1.9, 2.3$, or 2.8 the simulations are much simpler to understand. The pattern evolves to a looped labyrinthine state. This state is then fixed relative to a moving frame of reference, as the pattern simply moves up the solution domain at a constant rate (see Figure 7(b) as a prototypical example). This again can be compared with the single type boundary conditions in the previous two sections, where the patterns were stationary

In contrast to figures 7(a) and 7(b) the simulation illustrated in Figure 7(c) does not translate up or down the domain. Instead, we observe enclosed structures that oscillate between two states. For example if we label the subfigures of Figure 7(c) 1-5, left to right, respectively, then subfigures 1, 3 and 5 present one form of structure, whilst subfigures 2 and 4 illustrate the alternative oscillation form.

Finally, Figure 7(d), illustrates the most complex dynamics of all. Namely, the labyrinthine pattern is constantly evolving. Simultaneously the pattern undergoes a noticeable upwards drift.

In summary Section III A, Section III A 1 and Section III A 2 have illustrated that the patterns producible within the chiral chasing mechanism are incredibly complex. Moreover, the patterns depend heavily on the boundary conditions, spatial geometry and parameter values. This sensitivity to the noted factors appear to be more critical in the chasing mechanism than in a simple Turing pattern case, where, in general, it is seen that zero-flux boundary conditions often produce the same outcomes as periodic boundary conditions since zero-flux conditions are a subsymmetry of the periodic boundary conditions.

3. *Schnakenberg kinetics with diffusion*

In Section III A we saw that the Schnakenberg kinetics heavily restrict the angles that can lead to a patterning instability. In order to maximise the patterning domain we add in the assumption that the morphogens are allowed to diffuse with constant, positive diffusion rates, D_u and D_v, respectively. Further, we choose the diffusion rates to ensure that the system is Turing unstable to begin with. Hence, the chasing dynamic becomes a perturbation around the original Turing pattern and we can question how the pattern changes with the angle.

Specifically, we consider the equations

$$\begin{aligned}\frac{\partial u}{\partial t} &= D_u \nabla^2 u \\ &+ \frac{3Jr_1^2}{4}\nabla^2(uv) - r_1 J \nabla\cdot(u\boldsymbol{M}(\theta_1)\nabla v) \\ &+ \alpha - u + u^2 v - \epsilon u^3, \qquad (16)\\ \frac{\partial v}{\partial t} &= D_v \nabla^2 v \\ &+ \frac{3Jr_2^2}{4}\nabla^2(uv) + r_2 J \nabla\cdot(v\boldsymbol{M}(\theta_2)\nabla u) \\ &+ \beta - u^2 v - \epsilon v^3, \qquad (17)\end{aligned}$$

where, as before, $r_1 = 1$ and $r_2 = 2$. Note that although we will be also fixing $J = 1$ during the simulations of the equations we allow the variable to remain in the equations to illustrate its appearance in the conditions $P3$ and $P4$ and, further, illustrate that if $J = 0$ then the conditions simplify to the standard Turing conditions. The Fourier analysis in Appendix D can be applied nearly identically to equations (16) and (17). We note that conditions $P1$ and $P2$ are identical and that we can derive the following forms for $P3$ and $P4$:

$$P3: \quad 0 < \frac{J^2\beta(4\cos(\theta_1)\cos(\theta_2)+6\cos(\theta_1)-3\cos(\theta_2))}{2(\alpha+\beta)} + 3J\left(D_u(\alpha+\beta)+\frac{\beta D_v}{4(\alpha+\beta)^2}\right) + D_u D_v; \qquad (18)$$

$$P4: \quad \frac{J}{4}\left(8\cos(\theta_1)\beta + 8\cos(\theta_2)\beta - 15\beta + 12(\alpha+\beta)\right) + D_u(\alpha+\beta)^2 + D_v\frac{\alpha-\beta}{(\alpha+\beta)} < \qquad (19)$$

$$-2(\alpha+\beta)\sqrt{\frac{J^2\beta(4\cos(\theta_1)\cos(\theta_2)+6\cos(\theta_1)-3\cos(\theta_2))}{2(\alpha+\beta)} + 3J\left(D_u(\alpha+\beta)+\frac{\beta D_v}{4(\alpha+\beta)^2}\right) + D_u D_v}.$$

Figure 8(a) demonstrates that by adding diffusion into the equation many more values of (θ_1, θ_2) can drive the uniform steady state unstable, although the ‘small-θ_1-small-θ_2’ is still not valid. By increasing the ratio D_v/D_u the entire (θ_1, θ_2) parameter region can be made viable. However, in this case diffusion dominates the system and rotational chasing effects are not seen. Critically, what we have gained in (θ_1, θ_2) parameter space we have lost in the (α, β) parameter region (see Figure 8(b)). Here, we observe that the patterning region is now no longer unbounded. Moreover, although we are only showing the outcome for one set of (θ_1, θ_2) the size of the valid parameter region is only weakly dependent on these angles and not only does the valid region always stay bounded but it also hardly changes size as the angles are varied.

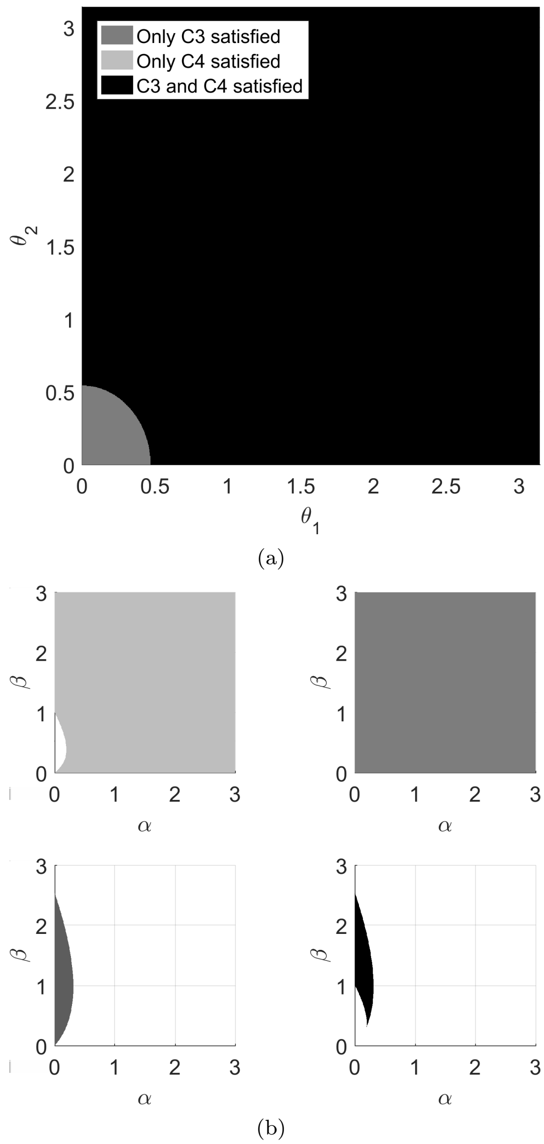

FIG. 8. Possible parameter regions for a patterning instability to occur in the Schnakenberg kinetics when diffusion is added. (a) The feasible (θ_1, θ_2) parameter region when $(\alpha, \beta) = (0.11, 0.9)$. (b) The feasible (α, β) regions (when $(\theta_1, \theta_2) = (1.8, 2.2)$) for $P1$ (top left), $P3$ (top right) and $P4$ (bottom left), respectively. The bottom right figure of (b) shows the intersection of the other three feasible regions. Note condition $P2$ is satisfied everywhere under these kinetics. Parameters are $J = 1$, $D_u = 1$ and $D_v = 22$.

The main point that we want to illustrate in this section is that we can theoretically reproduce the experimental trends discovered in [26]. Namely that the microscale chirality of the population agents can change the macroscale population pattern (see Figure 9) as we observe a transition from stripes to spots on all domains as θ_2 is varied. Further, we see the boundary geometry once again playing a large role in pattern selection and dynamics. Specifically, when $\theta_2 = -1.4$ the circle domain supports spot patterns, whereas the square domain produces stripes. Equally, all square domain patterns are stationary, whilst the patterns on the circle domains rotate. Notably, the direction of pattern rotation also appears to be dependent on θ_2, that is, the circular domain patterns spiral clockwise for $\theta_2 > -0.7$ and anticlockwise for $\theta_2 < -0.7$. Finally, we note that similar results occur if θ_1 is varied (simulations not shown), thus, these results are not special to the v population.

We close this section by illustrating one final result that demonstrates that stripes on a square domain are also able to undergo boundary rotations. Specifically, in Figure 10(a), we see ten time points in a simulation that shows that although the main vertical stripe pattern is stable there are boundary spots that rotate anticlockwise. Moreover, the dynamics repeat themselves because the pattern at time 4100 appears to match that at time 4600 and so the boundary densities are able to rotate around the domain in 500 time units.

B. Small angle patterns

Although we have shown that the angular chasing mechanism can generate patterns we have still to show that patterns can form in the 'small-θ_1-small-θ_2' region, which is perhaps the most realistically pertinent region of parameter space. In Appendix E we show that it is theoretically possible to generate patterns when $|\theta_1|, |\theta_2| < 1$. In this section we use those insights to provide two sets of kinetics that were produced on an ad-hoc basis to satisfy conditions $P1$-$P4$. Again, we note that we are not suggesting that these model a particular biological reaction, rather we are demonstrating the dynamics that the angular chasing framework can produce. Specifically, the reader can check that

$$f_1 = 1 + u^{1.9} - 2u^{0.9}v^2 - 10^{-6}u^2, \tag{20}$$

$$g_1 = 0.1 - 2.1v^{2.8} + 2u^3v^{1.59} - 10^{-6}v^2, \tag{21}$$

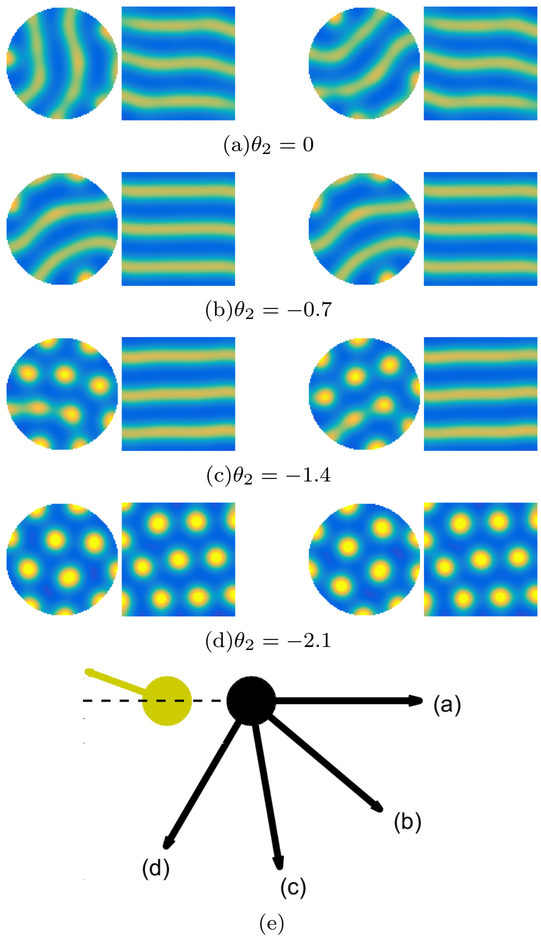

FIG. 9. The influence of angle on the pattern. Each simulation is done both on a circular and a square domain using Schnakenberg kinetics (with diffusion). The circle and square on the left of each subfigure are snapshots taken at time $t = 4500$, whilst those on the right are taken at time $t = 5000$. The two time points are to highlight which patterns are stationary and which are rotating. Namely, all circular patterns are rotating, whilst all square patterns are stationary. (e) illustrates the relative angles and distance of the cell movement in (a)-(d). Parameters are $J = 1$, $\alpha = 0.11$, $\beta = 1.1$ and $\theta_1 = 2.79$. The value of θ_2 is given beneath each subfigure. The circle has radius 10, the square has side length 20.

and

$$f_2 = 2.95 - u^{41/40} - 1.95\sqrt{u}v - 10^{-3}u^7, \quad (22)$$

$$g_2 = 2 - 2uv - 10^{-3}v^7. \quad (23)$$

satisfy the patterning conditions with steady states approximately equal to $(1, 1)$. The analogous (θ_1, θ_2) parameter regions are shown in Figure 11. Clearly, we observe that both sets of kinetics are predicted to evolve to spatial heterogeneity for values of $|\theta_1|, |\theta_2| < 1$.

Upon simulating kinetics f_1 and g_1 with $\theta_1 = 0.1 = \theta_2$ we find we can produce a spot patten on the circular domain (see Figure 12) in which the density of the morphogens never becomes stationary. Specifically, we observe that the spots continuously oscillate irregularly, with no apparent coupling between spots (see Figure 12(c)). Furthermore the spots on the boundary slowly rotate clockwise. Although proving such density oscillations are chaotic is outside the scope of this paper we should not be surprised that chaotic effects can be found by coupling the set of kinetics to the motion as it is well-known that chaotic Turing patterns can appear if the non-linearities of the interactions are chosen carefully [36].

Our final simulation, in Figure 13, of kinetics f_2 and g_2 illustrates points 2 and 7 of the list in Section II A. Specifically, patterns can form when $\theta_1 = \theta_2$ and for all combinations of $(\pm\theta_1, \pm\theta_2)$. Similar to the result seen in Figure 9, different angle values produce different patterns and directions of rotation. However, as we might expect, the system patterns are the same when both angles switch sign, although the direction of rotation is reversed. Namely, $(0.4, 0.4)$ and $(-0.4, -0.4)$ both produce labyrinthine patterns on the circle, but $(0.4, 0.4)$ rotates anticlockwise, whilst $(-0.4, -0.4)$ rotates in a clockwise manner. Similar observations can be made when the angles are $(0.4, -0.4)$ and $(-0.4, 0.4)$.

One critical note should be made when considering the patterns exhibited under the four angles $(\pm\theta_1, \pm\theta_2)$. Although the linear analysis suggests that in all four cases the uniform steady state becomes unstable in the same way this does not mean that the non-linear interactions will be able to stabilise a final pattern for all four angles. Indeed, many of the patterns produced in Section III A exhibit solution blow up instabilities if the signs of the angles are changed.

IV. SUMMARY AND CONCLUSION

In this paper we have been motivated by biological results on chiral cellular chasing to extend a deterministic integro-differential equation framework to include a rotational chasing mechanism. The framework was simplified through the use of multiple small limits leading to a coupled set of partial differential equations which

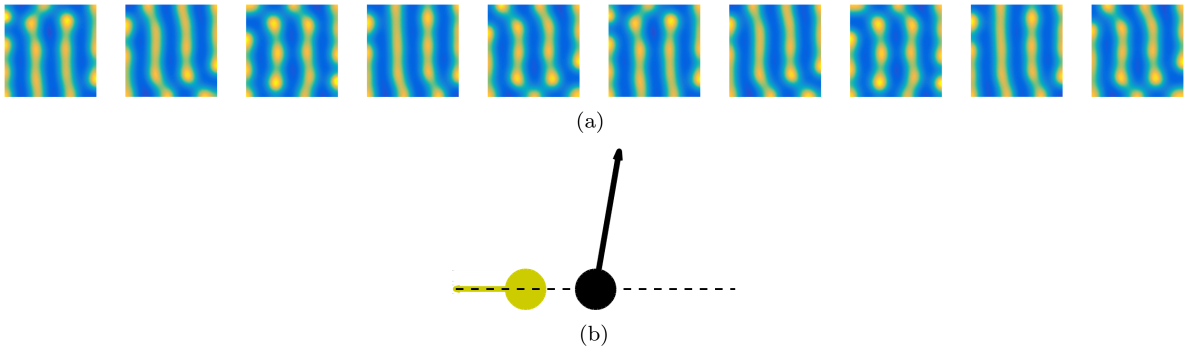

FIG. 10. Simulations of the Schnakenberg kinetics (with diffusion) at time points 4100 to 5000 in steps of 100 showing that the pattern on the boundary of the square domain rotates. If the pattern is simulated on a circle then the whole pattern rotates (simulations not shown). (b) illustrates the relative angles and distance of the cell movement. Parameters $\alpha = 0.11$, $\beta = 1.1$, $\theta_1 = 3.14$, $\theta_2 = 1.4$. The square has side length 20. See Supplemental Material at [URL will be inserted by publisher] for an animation of (a).

were amenable to standard Fourier analysis. By extending the derivation to include higher order derivatives, and by choosing the correct balance of parameters, it maybe possible to produce a system of PDEs, which have a non-trivial, bounded dispersion relation, without the need for extra kinetics. This is outside the scope of the current paper, but will be considered in future work.

The analytical and simulated results in sections II and III clearly demonstrate that the chiral chasing mechanism is able to destabilise a homogeneous steady state, similar to a Turing instability. However, the dependence of the instability conditions on the motion mechanism appear to be weaker than most Turing systems, which are well known for only patterning in small regions of parameter space [37].

The addition of this new motion type has enriched the complexity of the framework presented by Painter, Sherratt and co-authors [29, 30]. Specifically, a number of the patterns (see Figure 5) have never before been seen by the author. Further, although we may question the application of such new patterns to biological systems, the purpose of this article has not been to focus on a specific realistic application, but rather develop the underlying theory and demonstrate the wide variety of patterns available. Namely all of the known standard patterning solutions: spots; stripes; labyrinthine; etc. patterns are available with the added dynamics of stable spatial rotations. However, beyond the theoretical development of the framework, perhaps the most important applicable result we have produced is that our results corroborate the experimental idea that the global pigmentation pattern of a zebrafish's skin can be dependent on the chirality of the morphogens. Critically, due to the ad-hoc nature of the kinetics, the resulting insights generated in this paper only demonstrate that such micro- to macro-scale relationship can occur. In future work the author intends to focus on the specific case of the zebrafish chromatophore interactions and compare the data of wild-type and mutated fish with simulations produced from the theoretical framework constructed here.

Notably, although, the zebrafish's patterns do not generally move it has been shown through laser ablation experiments that the stripes can actively evolve to a steady state if their initial pattern is disrupted [21]. However, moving pigmentation patterns in fish are possible. The flamboyant cuttlefish, *metasepia pfefferi*, presents active moving stripes and spiral patterns in real time on its skin [38].

Due to the increased complexity of rotating patterns seen in this framework there are many further interesting questions to investigate regarding the chasing motion. For example, we have seen that the rotational speed and direction of the pattern appears to depend on the geometric angle of the chasing (see Figure 9). Equally, the influence of the boundary conditions and shape seem to be key. However, at the moment we need to rely on simulation in order to understand these non-linear effects. Thus, we look forward to investigating these and other questions arising from rotational chasing in the future.

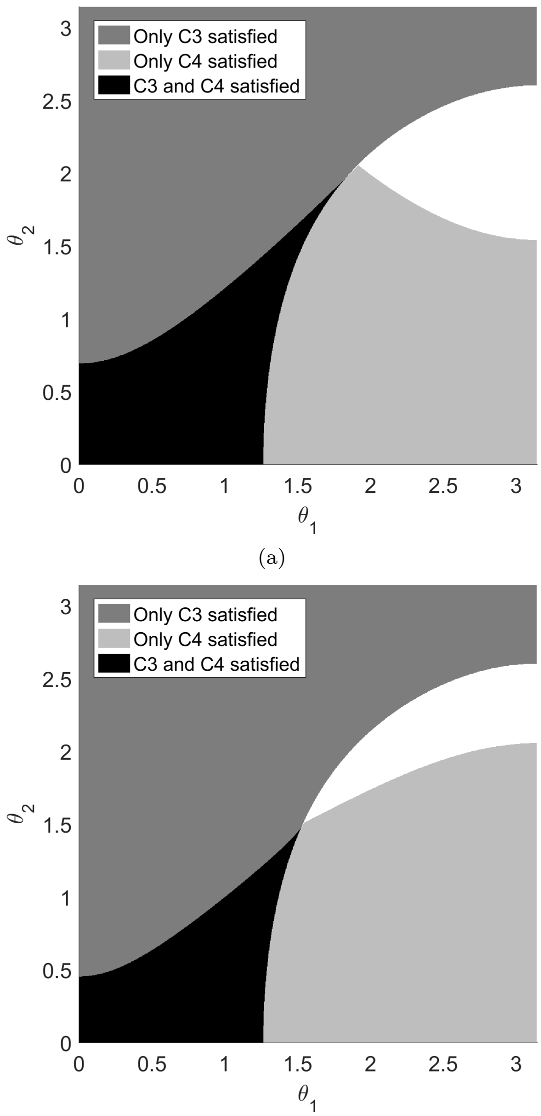

(a)

(b)

FIG. 11. Possible parameter regions for a patterning instability to occur when kinetic functions (a) f_1 and g_1 (equations (20) and (21)) and (b) f_2 and g_2 (equations (22) and (23)) are used.

V. ACKNOWLEDGEMENTS

TEW would like to thank St John's College, Oxford and the Mathematical Biosciences Institute (MBI) at Ohio State University, for financially supporting this research through the National Science Foundation grant DMS 1440386. TEW would also like to recognise the support of BBSRC grant BKNXBKOO BK00.16.

Appendix A: Diffusion equation derivation

The derivation that follows derives the diffusion equation in one dimension. Critically, the angular chasing mechanism that we will be considering needs a minimum of two-dimensions to be defined. Thus, we should note that we are only considering a one-dimensional diffusion derivation for simplicity and to illustrate the connection between a discretised system and its continuous analogue.

We consider a one-dimensional space, $[0, L]$, discretised into $N \in \mathbb{N}$ intervals of equal size, $\delta_x = L/N$. Note that extending the derivation to higher dimensions is trivial, but algebraically cumbersome. Each interval, $i = 1, \ldots, N$, contains a density $u_i = u((i-1/2)\delta_x)$, which is defined to be in the centre of each interval. Each population is able to undergo an unbiased random walk, with rate d. This can be written as a set of interaction equations,

$$u_1 \underset{d}{\overset{d}{\rightleftharpoons}} u_2 \underset{d}{\overset{d}{\rightleftharpoons}} \ldots \underset{d}{\overset{d}{\rightleftharpoons}} u_{N-1} \underset{d}{\overset{d}{\rightleftharpoons}} u_N. \tag{A1}$$

These equations assume that the boundaries are reflective and that nothing can leave the domain. Thus, the system has zero-flux boundary conditions.

Using the Law of Mass Action on equation (A1) we are able to derive the following system of coupled ordinary differential equations, which define the evolution of each continuous population:

$$\frac{\mathrm{d}u_1}{\mathrm{d}t} = d\left(u_2 - u_1\right), \tag{A2}$$

$$\frac{\mathrm{d}u_i}{\mathrm{d}t} = d\left(u_{i-1} - 2u_i + u_{i+1}\right), \quad i = 2, \ldots, N-1, \tag{A3}$$

$$\frac{\mathrm{d}u_N}{\mathrm{d}t} = d\left(u_{N-1} - u_N\right). \tag{A4}$$

Upon taking the limit $\delta_x \to 0$ and requiring $D = d\delta_x^2$ to be finite, we derive the standard partial differential equation representation of the diffusion equation,

$$\frac{\partial u}{\partial t} = D\frac{\partial^2 u}{\partial x^2}, \tag{A5}$$

$$\frac{\partial u}{\partial x} = 0, \quad x = 0, L. \tag{A6}$$

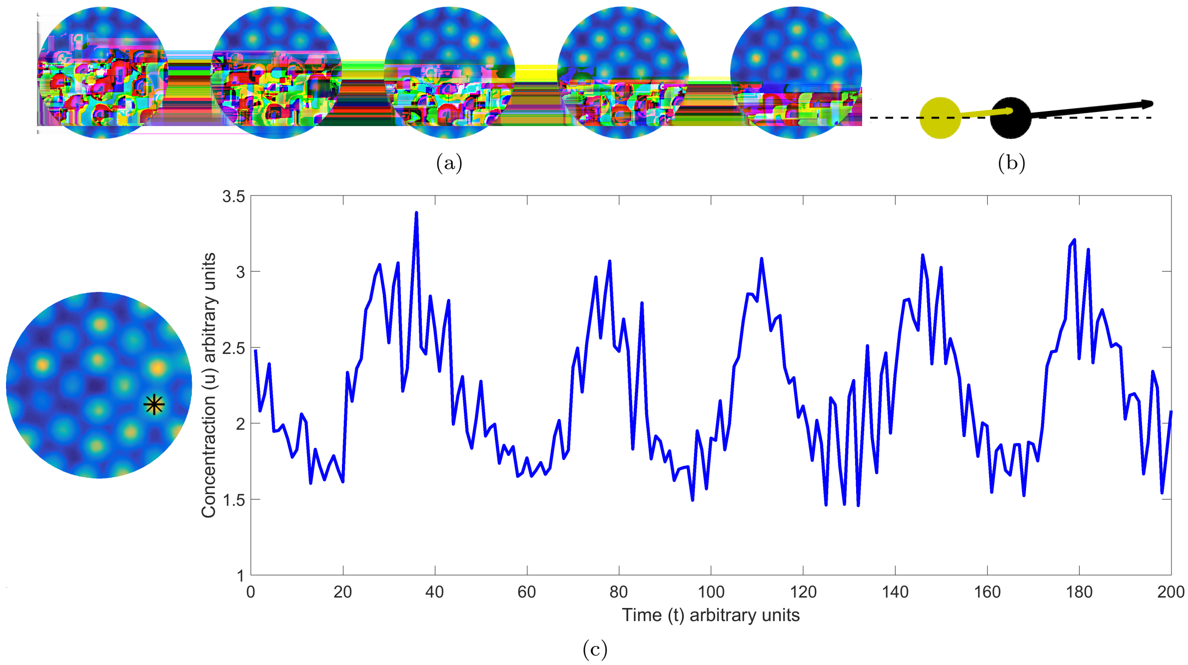

FIG. 12. 'Twinkling spots' of density oscillations, with rotating boundary spots can be produced from the angular chasing mechanism. (a) Consecutive time points taken every one arbitrary unit of time illustrating the twinkling spot pattern. (b) illustrates the relative angles and distance of the cell movement. (c) Concentration trace over time of a single point. The point is marked with an asterisk in the left pattern and the chosen point is the centre of a spot. Parameters $\theta_1 = 0.1 = \theta_2$. The circle's radius is 10. See Supplemental Material at [URL will be inserted by publisher] for an animation of (a).

Appendix B: Detailed derivation of chiral chasing equations

Considering Figure 1 and assuming that all interactions have the same propensity rate, $j > 0$, then all fluxes to and from a point (x, y) can be written in terms of similar interaction equations:

$$u(x - r_{1x}, y - r_{1y}) + v(x - r_{1x} + r\cos(\alpha), y - r_{1y} + r\sin(\alpha)) \xrightarrow{j} u(x, y)+ \\ v(x - r_{1x} + r\cos(\alpha) + r_{2x}, y - r_{1y} + r\sin(\alpha) + r_{2y}); \tag{B1}$$

$$u(x - r\cos(\alpha), y - r\sin(\alpha)) + v(x, y) \xrightarrow{j} u(x - r\cos(\alpha) + r_{1x}, y - r\sin(\alpha) + r_{1y})+ \\ v(x + r_{2x}, y + r_{2y}); \tag{B2}$$

$$u(x - r\cos(\alpha) - r_{2x}, y - r\sin(\alpha) - r_{2y}) + v(x - r_{2x}, y - r_{2y}) \xrightarrow{j} v(x, y)+ \\ u(x - r\cos(\alpha) + r_{1x} - r_{2x}, y - r\sin(\alpha) + r_{1y} - r_{2y}). \tag{B3}$$

In terms of meaning: equations (1) and (B1) are the equations governing the rate at which u moves from and to the position (x, y), respectively; equations (B2) and (B3) are the analogous

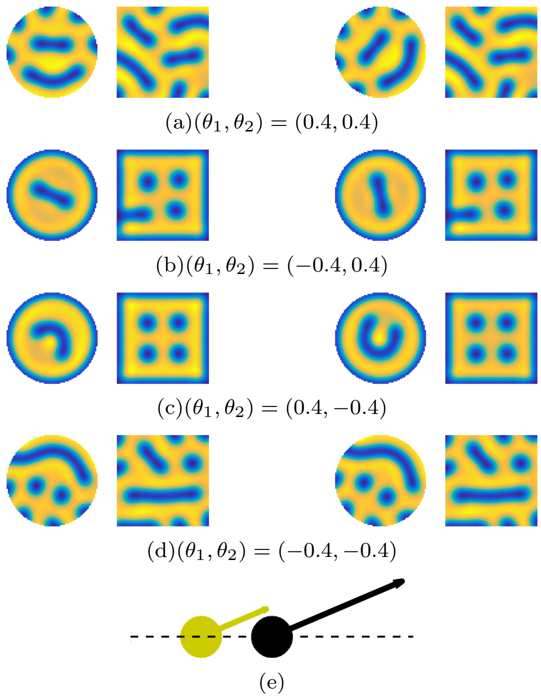

FIG. 13. Influence of angle sign on pattern. Each simulation is identical except for the values of (θ_1, θ_2), which are specified in the subcaption of each figure, respectively. Two time points are shown for each simulation, namely the figures on the left are at $t = 3500$, whilst the figures on the right are at $t = 5000$. This illustrates the rotation of the patterns on the circular domains. (e) illustrates the relative angles and distance of the cell movement in (a). The relative angle and distances for (b)-(c) are simply appropriate reflections of the arrows in the horizontal dashed line. The circle's radius is 10 and the square has side length 20.

equations for the v population.

Using the Law of Mass Action, the evolution equations can then be rewritten in terms of integro-differential equations,

$$\frac{\partial u}{\partial t} = \int_0^{2\pi}\int_0^R [-u(x,y)v(x + r\cos(\alpha), y + r\sin(\alpha)) + u(x - r_{1x}, y - r_{1y})\times v(x - r_{1x} + r\cos(\alpha), y - r_{1y} + r\sin(\alpha))]\, jr \text{ d}r \text{ d}\alpha, \tag{B4}$$

$$\frac{\partial v}{\partial t} = \int_0^{2\pi}\int_0^R [-u(x - r\cos(\alpha), y - r\sin(\alpha))v(x,y) + v(x - r_{2x}, y - r_{2y})\times u(x - r\cos(\alpha) - r_{2x}, y - r\sin(\alpha) - r_{2y})]\, jr \text{ d}r \text{ d}\alpha. \tag{B5}$$

Next, we take the limits $\delta_x, \delta_y \to 0$ with the further constraint that $\delta_x = \delta_y = \delta_s$ and j is chosen such that $J = j\delta_s$ remains finite.

Specifically, the integrals in equations (B4) and (B5) calculate the net flux of the u and v populations into a point (x, y), respectively. Further the variables r_{il}, $i \in \{1, 2\}$, $l \in \{x, y\}$, are defined to be $r_{1x} = r_1\delta_x\cos(\theta_1)$, $r_{1y} = r_1\delta_y\sin(\theta_1)$,

$r_{2x} = r_2\delta_x \cos(\theta_2)$ and $r_{2y} = r_2\delta_y \cos(\theta_2)$.

Assuming δ_x and δ_y are small we derive a multiseries expansion of equations (B4) and (B5) up to first order. Specifically, equation (B4) becomes

$$\begin{aligned}\frac{\partial u}{\partial t} = \int_0^{2\pi}\int_0^R & -\cos(\alpha+\theta_1)\, jrr_1\delta_x \left(\frac{\partial u}{\partial x}(x,y)\, v(x+r\cos(\alpha), y+r\sin(\alpha))\right. \\ & \left. +u(x,y)\frac{\partial v}{\partial x}(x+r\cos(\alpha), y+r\sin(\alpha))\right) \\ & -\sin(\alpha+\theta_1)\, jrr_1\delta_y \left(\frac{\partial u}{\partial y}(x,y)\, v(x+r\cos(\alpha), y+r\sin(\alpha))\right. \\ & \left. +\frac{\partial v}{\partial y}(x+r\cos(\alpha), y+r\sin(\alpha))\, u(x,y)\right) + \mathcal{O}\left(\delta_x^2, \delta_y^2, \delta_x\delta_y\right) \mathrm{d}r\mathrm{d}\alpha.\end{aligned} \tag{B6}$$

We now fix $\delta_x = \delta_y = \delta_s$, define $J = j\delta_s$ and let $\delta_s \to 0$. Upon simplification we derive

$$\frac{\partial u}{\partial t} = -r_1 J \int_0^{2\pi}\int_0^R \begin{pmatrix}\cos(\alpha+\theta_1)\\ \sin(\alpha+\theta_1)\end{pmatrix} \cdot \nabla\left(u(x,y)v(x+r\cos(\alpha))\right) r\ \mathrm{d}r\ \mathrm{d}\alpha. \tag{B7}$$

$$\tag{B8}$$

If equation (B5) is handled in the same way then we derive.

$$\frac{\partial v}{\partial t} = -r_2 J \int_0^{2\pi}\int_0^R \begin{pmatrix}\cos(\alpha-\theta_2)\\ \sin(\alpha-\theta_2)\end{pmatrix} \cdot \nabla\left(v(x,y)u(x-r\cos(\alpha))\right) r\ \mathrm{d}r\ \mathrm{d}\alpha. \tag{B9}$$

In the case that $\theta_1 = \theta_2 = 0$ we reduce to the previously derived equations from [29, 30] with appropriate choices of integral kernel and additional local term.

Appendix C: Expanding in terms on R, δ_x and δ_y

In order to simplify the equations produced in Appendix B further we also take the limit of small detection radius. Namely, we return to equation (B4) and Taylor expand the equation up to order four in R, δ_x and δ_y, in order to give

$$\frac{\partial u}{\partial t} = \frac{\pi R^3 j r_1}{3}\left(\left(v_{xy}u + v_y u_x\right)\delta_x - \left(v_{xy}u + v_x u_y\right)\delta_y\right)\sin\left(\theta_1\right) - \frac{\pi R^3 j r_1}{3}\left(\left(u v_{xx} + u_x v_x\right)\delta_x + \left(u v_{yy} + u_y v_y\right)\delta_y\right)\cos\left(\theta_1\right) + \frac{\pi R^2 j {r_1}^2}{4}\left(\left(u v_{xx} + u_{xx} v + 2u_x v_x\right){\delta_x}^2 + \left(u v_{yy} + u_{yy} v + 2u_y v_y\right){\delta_y}^2\right) + \mathcal{O}\left(R^{i_1}\delta_x^{i_2}\delta_y^{i_3}\right), \quad \text{(C1)}$$

where $i_1 + i_2 + i_3 > 4$. For the sake of brevity, we have suppressed the arguments, (x, y, t), and written all spatial derivatives as underscores.

We intend to take the limit of $R = \delta_x = \delta_y = \delta_s$ tending to zero, however, we specify that j be chosen such that $J = \delta_s^4 j\pi/3$ remains constant. Hence, substituting δ_s and J into the equations and taking the limit $\delta_s \to 0$, we derive (3). The equation for v can be produced analogously and is shown in (4).

Appendix D: Stability conditions arising from linearising about a homogeneous steady state

The following analysis all takes place on an infinite domain, thus, we begin by defining the perturbation

$$u = u_0 + e_u \exp(I\boldsymbol{k}\cdot\boldsymbol{x} + \lambda t), \quad \text{(D1)}$$

$$v = v_0 + e_v \exp(I\boldsymbol{k}\cdot\boldsymbol{x} + \lambda t), \quad \text{(D2)}$$

where I is the standard imaginary unit, $\boldsymbol{k} = (k_x, k_y)^T$ is a general wave mode from the solution's Fourier expansion, $\boldsymbol{x} = (x, y)^T$ is the regular Cartesian coordinate vector, e_u and e_v are general constants that control the size of the initial perturbation, so we assume that $0 < |e_u|, |e_v| \ll 1$, and λ defines the stability of the steady state. From the above assumptions, when $J = 0$ we require that all possible values of λ have negative real part, whilst when $J > 0$ we require that there is at least one viable value of λ that has positive real part. Finally, we note that, by combining the spatial perturbation into the exponential equation we are assuming that the system is being simulated on an infinite domain. Other boundary conditions can be accounted for by altering the perturbation form [9].

Substituting equations (D1) and (D2) into equations (3) and (4), with reaction terms f and g added to the u and v equations, respectively, and expanding each equation to linear order we can turn the two resulting linear relationships into a single matrix equation,

$$\begin{pmatrix} -\lambda + f_u - 3Jk^2 r_1^2 v_0/4 & Jk^2 r_1 u_0\left(\cos(\theta_1) - 3r_1/4\right) + f_v \\ -Jk^2 r_2 v_0\left(\cos(\theta_2) - 3r_2/4\right) + g_u & -\lambda + g_v - 3Jk^2 r_2^2 u_0/4 \end{pmatrix}\begin{pmatrix} e_1 \\ e_2 \end{pmatrix} = \mathbf{0}, \quad \text{(D3)}$$

where $f_i, i \in \{u, v\}$ represents the partial derivative of f, with respect to i and then evaluated at the steady state. The $g_i, i \in \{u, v\}$ are similarly defined.

In order for a non-trivial solution of $(e_1, e_2)^T$ to exist the matrix in equation (D3) must be singular and the problem of stability converts to a problem of finding null-eigenvalues, λ, of equation (D3). Setting the determinant of the matrix to zero we derive the dispersion relation,

$$\lambda^2 + \left(\left({r_1}^2 v_0 + r_2^2 u_0\right)\frac{3Jk^2}{4} - f_u - g_v\right)\lambda + h(k^2), \quad \text{(D4)}$$

where

$$h(k^2) = \left(4\cos(\theta_1)\cos(\theta_2) - 3r_1\cos(\theta_2) + 3\cos(\theta_1)\,r_2\right)\frac{r_1 r_2 u_0 v_0 J^2 k^4}{4}$$
$$+ \left(\left(r_2\left(4\cos(\theta_2) + 3r_2\right)f_v - 3{r_1}^2 g_v\right)v_0 - \left(r_1\left(4\cos(\theta_1) + 3r_1\right)g_u - 3f_u{r_2}^2\right)u_0\right)\frac{Jk^2}{4} + f_u g_v - f_v g_u. \tag{D5}$$

In order to ensure that the roots of equation (D4) have negative real part when $J = 0$ it is necessary and sufficient for the constant term, $h(k^2)$, and the coefficient of λ to be positive. Hence, for stability in the absence of motion, $J = 0$, we must have

$$f_u + g_v < 0 \tag{D6}$$
$$f_u g_v - f_v g_u > 0, \tag{D7}$$

which, unsurprisingly, match the initial Turing conditions without diffusion. We denote these conditions $P1$ and $P2$, respectively. In the case that $J > 0$ we desire that an instability exists. Thus, either the constant term, $h(k^2)$, or the coefficient of λ must be negative, for some value of k. Since the term

$$\left({r_1}^2 v_0 + r_2^2 u_0\right)\frac{3Jk^2}{4} \tag{D8}$$

is guaranteed to be positive (as we are assuming that the steady states are realistic and, thus, non-negative) then we deduce that the coefficient of λ must always be positive. Hence, the only way to drive the system to instability is if $h(k^2) < 0$, for some $k^2 > 0$.

We, firstly, note that $h(k^2)$ is quadratic in k^2. Thus, for large enough k, the sign of h will be determined by the sign of the coefficient of k^4. In order to stop arbitrarily small wavelengths from growing and breaking a simulation down to just noise (simulations not shown), we require that the unstable wave modes should be bounded above, meaning that $h(k^2)$ should be positive for large $k > 0$ and, so, we require

$$4\cos(\theta_1)\cos(\theta_2) - 3r_1\cos(\theta_2) + 3\cos(\theta_1)\,r_2 > 0, \tag{D9}$$

This inequality is denoted condition $P3$.

Having specified the problem to ensure that $h(k^2)$ has positive leading order polynomial term we now require that the quartic becomes negative for a non-trivial interval of k. This means that not only do we want at least two roots of the quartic h to have a positive real part, but we also demand that the roots are real at the bifurcation point. Treating the equation as a quadratic in k^2 and considering the binomial formula we conclude that we need the discriminant to be positive and the coefficient of k^2 to be negative. These two conditions can be wrapped up into a single inequality,

$$\left(\left(r_2\left(4\cos(\theta_2) + 3r_2\right)f_v - 3{r_1}^2 g_v\right)\frac{v_0}{4} - \left(r_1\left(4\cos(\theta_1) - 3r_1\right)g_u + 3f_u{r_2}^2\right)\frac{u_0}{4}\right) < \tag{D10}$$
$$- \sqrt{r_1 r_2\left(4\cos(\theta_1)\cos(\theta_2) + 3\cos(\theta_1)\,r_2 - 3r_1\cos(\theta_2)\right)u_0 v_0\left(f_u g_v - f_v g_u\right)},$$

which is denoted condition $P4$.

Appendix E: Small angle derivation

In this section we further simplify the conditions derived in Appendix D under the assumption that we are looking for solutions with only small values of θ_1 and θ_2. This section is needed because from simulation experience (as seen in Section III) some of the common patterning kinetics tend to rule out small angle solutions, as they require $\theta_1,\ \theta_2 > \pi/2$. Hence, we want to show that such small angle patterns are (at least theoretically) possible in order to match the results in [26], where a number of the deviating angles were less than 1 rad.

Firstly, inequalities (D6) and (D7) are independent of the angles and, so, they remain the same regardless the values of (θ_1, θ_2). Further, since the equations all contain only cosine functions then the leading order correction will come in at the order of $\theta_i^2, i \in \{1, 2\}$, thus, linearised equations will eliminate all angular terms. Expanding inequality (D9) about $\theta_1 = \theta_2 = 0$ we see that the condition to be satisfied is simply

$$r_1 < \frac{4}{3} + r_2. \tag{E1}$$

Hence, we can see that, although the chaser cells, u, can move further than the escaping cells, v, during each interaction, their movement is bounded above, whereas the movement range of the v population is not.

Condition $P4$ is not so easy to simplify and, thus, we show that small angle patterned solutions are possible by appealing to a specific simplified form of the kinetics, namely,

$$f = 1 + f_u u + f_v v, \tag{E2}$$
$$g = 1 + g_u u + g_v v, \tag{E3}$$

where we further assume that $f_v,\ g_u > 0$, to ensure the positivity of the homogeneous steady state solution and we fix $r_1 = 1$ and $r_2 = 2$ to reduce the number of free parameters. Note that because we are only dealing with linear kinetics any motion-driven instability will grow without bound. However, once we have derived a system that is driven unstable by motion we can add non-linearities, multiplied by small factors. These non-linearities are designed to keep the solution bounded, and the small multiplicative factors ensure that they will not greatly influence the prior linear analysis, that is, we are in the weakly non-linear regime.

Substituting equations (E2) and (E3) into conditions $P1$-$P4$ and linearising with respect to θ_1 and θ_2 generates four inequalities. We insert these inequalities along with the constraints $u_0, v_0 > 0$ into an algebraic manipulation package in order to see if there are non-trivial parameter regions in which the conditions can all be satisfied. Critically, there are many possible parameter regions that satisfy the conditions, thus, there are plenty of possible values of (f_u, f_v, g_u, g_v) to choose from, even with the large number of constraints we have placed on the solution. For example, one particular simple set of kinetics have the generic form

$$-12 f_v = g_v < 0, \tag{E4}$$
$$f_u < -\frac{69 g_u}{100}, \tag{E5}$$
$$0 < g_u < -\frac{656 g_v}{3191}. \tag{E6}$$

[1] T. E. Woolley, R. E. Baker, C. Tickle, P. K. Maini, and M. Towers. Mathematical modelling of digit specification by a sonic hedgehog gradient. *Dev. Dynam.*, 243(2):290–298, 2014.

[2] T. E. Woolley, R. E. Baker, P. K. Maini, J. L. Aragón, and R. A. Barrio. Analysis of stationary droplets in a generic Turing reaction-diffusion system. *Phys. Rev. E*, 82(5):051929, 2010.

[3] P. K. Maini, T. E. Woolley, E. A. Gaffney, and R. E. Baker. *The Once and Future Turing*, chapter 15: Biological pattern formation. Cambridge University Press, 2016.

[4] M. C. Cross and P. C. Hohenberg. Pattern formation outside of equilibrium. *Rev. Mod. Phys.*, 65(3):851–1112, 1993.

[5] J. S. Langer. Instabilities and pattern formation in crystal growth. *Rev. Mod. Phys.*, 52(1): 1, 1980.

[6] J. A Glazier and D. Weaire. The kinetics of cellular patterns. *J. Phys.: Condens. Matter*, 4(8): 1867, 1992.

[7] A. M. Turing. The chemical basis of morphogenesis. *Phil. Trans. R. Soc. Lond. B*, 237:37–72, 1952.

[8] T. E. Woolley. *50 Visions of Mathematics*, chapter 48: Mighty Morphogenesis. Oxford Univ. Press, 2014.

[9] J. D. Murray. *Mathematical Biology II: Spatial Models and Biomedical Applications*, volume 2. Springer-Verlag, 3rd edition, 2003.

[10] T. E. Woolley, R. E. Baker, and P. K. Maini. *The Turing Guide*, chapter 35: Turing's theory of morphogenesis. Oxford Univ. Press, To appear 2017.

[11] P. K. Maini, T. E. Woolley, R. E. Baker, E. A. Gaffney, and S. S. Lee. Turing's model for biological pattern formation and the robustness problem. *Interface Focus*, 2(4):487–496, 2012.

[12] V. Klika, R. E. Baker, D. Headon, and E. A. Gaffney. The Influence of Receptor-Mediated Interactions on Reaction-Diffusion Mechanisms of Cellular Self-organisation. *B. Math. Biol.*, 74(4):

935–957, 2012.
[13] S. Seirin Lee and E. A. Gaffney. Aberrant behaviours of reaction diffusion self-organisation models on growing domains in the presence of gene expression time delays. *Bull. Math. Biol.*, 72:2161–2179, 2010.
[14] T. E. Woolley, R. E. Baker, E. A. Gaffney, and P. K. Maini. Influence of stochastic domain growth on pattern nucleation for diffusive systems with internal noise. *Phys. Rev. E*, 84(4): 041905, 2011.
[15] T. E. Woolley, R. E. Baker, E. A. Gaffney, P. K. Maini, and S. Seirin-Lee. Effects of intrinsic stochasticity on delayed reaction-diffusion patterning systems. *Phys. Rev. E*, 85(5):051914, 2012.
[16] L. Marcon, X. Diego, J. Sharpe, and P. Müller. High-throughput mathematical analysis identifies Turing networks for patterning with equally diffusing signals. *eLife*, 5:e14022, 2016.
[17] M. F. Adamer, T. E. Woolley, and H. A. Harrington. Graph-Facilitated Resonant Mode Counting in Stochastic Interaction Networks. *arXiv preprint arXiv:1702.08747*, 2017.
[18] E. V. Entchev, A. Schwabedissen, and M. González-Gaitán. Gradient formation of the TGF-β homolog Dpp. *Cell*, 103(6): 981–992, 2000.
[19] S. Sick, S. Reinker, J. Timmer, and T. Schlake. WNT and DKK determine hair follicle spacing through a reaction-diffusion mechanism. *Science*, 314(5804):1447–1450, 2006.
[20] A. D. Economou, A. Ohazama, T. Porntaveetus, P. T. Sharpe, S. Kondo, M.A. Basson, A. Gritli-Linde, M. T. Cobourne, and J. B. A. Green. Periodic stripe formation by a Turing mechanism operating at growth zones in the mammalian palate. *Nat. Genet.*, pages 1546–1718, 2012.
[21] M. Yamaguchi, E. Yoshimoto, and S. Kondo. Pattern regulation in the stripe of zebrafish suggests an underlying dynamic and autonomous mechanism. *Proc. Nat. Acad. Sci.*, 104(12):4790–4793, 2007.
[22] A. Nakamasu, G. Takahashi, A. Kanbe, and S. Kondo. Interactions between zebrafish pigment cells responsible for the generation of Turing patterns. *Proc. Nat. Acad. Sci.*, 106(21): 8429–8434, 2009.
[23] H. G. Frohnhöfer, J. Krauss, H.-M. Maischein, and C. Nüsslein-Volhard. Iridophores and their interactions with other chromatophores are required for stripe formation in zebrafish. *Development*, 140(14):2997–3007, 2013.
[24] S. Kondo. The reaction-diffusion system: a mechanism for autonomous pattern formation in the animal skin. *Genes. Cells.*, 7(6):535–541, 2002.
[25] M. Hirata, K. Nakamura, and S. Kondo. Pigment cell distributions in different tissues of the zebrafish, with special reference to the striped pigment pattern. *Dev. Dynam.*, 234(2):293–300, 2005.
[26] H. Yamanaka and S. Kondo. In vitro analysis suggests that difference in cell movement during direct interaction can generate various pigment patterns in vivo. *Proc. Nat. Acad. Sci.*, 111(5): 1867–1872, 2014.
[27] T. E. Woolley, P. K. Maini, and E. A. Gaffney. Is pigment cell pattern formation in zebrafish a game of cops and robbers? *Pig. Cell Melan. Res.*, 27(5):686–687, 2014.
[28] H. Yamanaka and S. Kondo. Rotating pigment cells exhibit an intrinsic chirality. *Genes to Cells*, 20(1):29–35, 2015.
[29] N. J. Armstrong, K. J. Painter, and J. A. Sherratt. A continuum approach to modelling cell–cell adhesion. *J. Theor. Biol.*, 243(1):98–113, 2006.
[30] K. J. Painter, J. M. Bloomfield, J. A. Sherratt, and A. Gerisch. A nonlocal model for contact attraction and repulsion in heterogeneous cell populations. *Bull. Math. Biol.*, 77(6):1132–1165, 2015.
[31] S. Kondo. Cell-Cell Interaction Network That Generates the Skin Pattern of Animal. *Gen. Inform.*, 16(2):287, 2005.
[32] A. Buttenschoen, T. Hillen, A. Gerisch, and K. Painter. A space-jump derivation for non-local models of cell-cell adhesion and non-local chemotaxis. *bioRxiv*, page 093617, 2016.
[33] N. G. van Kampen. *Stochastic Processes in Physics and Chemistry.* North Holland, 3rd edition, 2007.
[34] J. Schnakenberg. Simple chemical reaction systems with limit cycle behaviour. *J. Theor. Biol.*, 81(3):389–400, 1979.
[35] T. E. Woolley. *Spatiotemporal Behaviour of Stochastic and Continuum Models for Biological Signalling on Stationary and Growing Domains.* PhD thesis, University of Oxford, 2011.
[36] J. L. Aragón, R. A. Barrio, T. E. Woolley, R. E. Baker, and P. K. Maini. Nonlinear effects on Turing patterns: Time oscillations and chaos. *Phys. Rev. E*, 86(2):026201, 2012.
[37] J. D. Murray. Parameter space for Turing instability in reaction diffusion mechanisms: a comparison of models. *J. Theor. Biol.*, 98(1):143, 1982.
[38] K. V. Langridge. Cuttlefish use startle displays, but not against large predators. *Anim. Behav.*, 77(4):847–856, 2009.